

Bottom-up Fabrication and Atomic-scale Characterization of Triply-linked, Laterally π -Extended Porphyrin Nanotapes

Qiang Sun (✉ qiangsun@shu.edu.cn)

Shanghai University <https://orcid.org/0000-0003-4903-4570>

Luis Mateo

Universidad Autónoma de Madrid

Roberto Robles

Centro de Física de Materiales CFM/MPC (CSIC-UPV/EHU)

Nicolas Lorente

Centro de Física de Materiales CFM/MPC (CSIC-UPV/EHU)

Pascal Ruffieux

Swiss Federal Laboratories for Materials Science and Technology <https://orcid.org/0000-0001-5729-5354>

Giovanni Bottari

Universidad Autónoma de Madrid <https://orcid.org/0000-0001-6141-7027>

Tomas Torres

Universidad Autónoma de Madrid <https://orcid.org/0000-0001-9335-6935>

Roman Fasel

Swiss Federal Laboratories for Materials Science and Technology <https://orcid.org/0000-0002-1553-6487>

Article

Keywords: Porphyrin nanotapes (Por NTs), molecular wires, electronic properties

Posted Date: March 1st, 2021

DOI: <https://doi.org/10.21203/rs.3.rs-284564/v1>

License:   This work is licensed under a Creative Commons Attribution 4.0 International License.

[Read Full License](#)

Bottom-up Fabrication and Atomic-scale Characterization of Triply-linked, Laterally π -Extended Porphyrin Nanotapes

Qiang Sun,^{‡,¶} Luis M. Mateo,^{†,‡,¶} Roberto Robles,^{‡,¶} Nicolas Lorente,^{‡,¶,*} Pascal Ruffieux,[‡] Giovanni Bottari,^{*,†,‡,§} Tomás Torres^{*,†,‡,§} and Roman Fasel^{*,‡,†}

[‡] nanotech@surfaces Laboratory, Empa-Swiss Federal Laboratories for Materials Science and Technology, 8600 Dübendorf, Switzerland.

[†] Departamento de Química Orgánica, Universidad Autónoma de Madrid, 28049 Madrid, Spain.

[‡] IMDEA-Nanociencia, Campus de Cantoblanco, 28049 Madrid, Spain.

[‡] Centro de Física de Materiales CFM/MPC (CSIC-UPV/EHU), Paseo de Manuel de Lardizabal 5, 20018 Donostia-San Sebastián, Spain.

[°] Donostia International Physics Center (DIPC), 20018 Donostia-San Sebastián, Spain.

[§] Institute for Advanced Research in Chemical Sciences (IAdChem), Universidad Autónoma de Madrid, 28049 Madrid, Spain.

[‡] Materials Genome Institute, Shanghai University, 200444 Shanghai, China.

⁺ Department of Chemistry and Biochemistry, University of Bern, 3012 Bern, Switzerland.

[¶] These authors contributed equally to the paper.

*Corresponding author: roman.fasel@empa.ch (R.F.); tomas.torres@uam.es (T.T); giovanni.bottari@uam.es (G.B.); nicolas.lorente@ehu.eus (N.L.)

Porphyrin nanotapes (Por NTs) have attracted vast interest as potential molecular wires thanks to their high degree of π -conjugation, low HOMO-LUMO gaps, and exceptional conductance, which increases with length. Recently, Por NTs have been synthesized by solution-based methods, demonstrating high versatility and great potential for technological applications. However, their synthesis is tedious and their characterization limited by low solubility and stability. Here, we report the first example of *meso-meso* triply-fused Por NTs, which are prepared from a readily available Por precursor through a two-step synthesis on Au(111). The diradical character of the on-surface formed building block PorA₂, a phenalenyl π -extended Zn(II)Por, facilitates intermolecular homocoupling and allows for the formation of laterally π -extended tapes. The structural and electronic properties of individual Por NTs are addressed, both on Au(111) and on a thin insulating NaCl layer, by high-resolution scanning probe

microscopy/spectroscopy complemented by density functional theory calculations. Remarkably, the triply-linked, laterally π -extended Por NTs carry one unpaired electron at each end, which leads to magnetic end states. Our study provides an alternative and versatile route to the fabrication of Por NTs and the atomic-scale characterizations of their structural and electronic properties.

Tetrapyrroles, “the pigments of life”, are key molecules for the metabolism of living organisms, supporting functions of vital importance such as electron transport, light-harvesting and oxygen reduction¹. Within this family of compounds, porphyrins (Pors) are of particular interest thanks to their planar structure with an aromatic core of 18 π -electrons, remarkable thermal stability, tunable redox properties, and intense optical features¹. Taking advantage of these properties and the Pors’ extraordinary chemical versatility, these macrocycles have been tailored for their use in a wide range of fields, such as photovoltaics², catalysis³ and molecular electronics⁴, to mention a few.

In the field of organic semiconductors and molecular electronics, π -extended Por monomers and, in particular, oligomers, have gained considerable attention as potential molecular wires^{5,6}, near-infrared absorbers, and nonlinear optical components due to their low highest occupied molecular orbital (HOMO) - lowest unoccupied molecular orbital (LUMO) gaps arising from their large π -conjugated structure⁷. Furthermore, the inner cavity of Pors can chelate transition metal ions which allows for the construction of magnetically-active nanostructures, such as organic spin filters⁸.

Focusing on Por oligomers, it has been demonstrated that the nature of the Por-Por linkage dramatically affects the electronic properties⁹. In particular, the number (*i.e.*, singly-, doubly-, or triply-connected)¹⁰ and the site (*i.e.*, β - β , *meso*- β , and/or *meso-meso*) of the inter-Por connectivity¹¹ as well as the chemical nature of the linker (*e.g.*, C-C single bond, and/or π -spacers)¹² have been identified as key factors. In this context, it was shown that the highest degree of π -conjugation and lowest HOMO-LUMO gaps were achieved by the *meso-meso*, β - β , β - β triple linkage, which leads to planar, fused Por oligomers^{13,14}. Such triply-fused Por oligomers show remarkable transport properties^{6,15} compared to typical “benchmark” systems like oligophenylenevinylene¹⁶, oligothiophene¹⁷ and oligoynes¹⁸.

Up to date, triply-fused Pors have been obtained in solution through oxidative ring closure of their corresponding *meso-meso* linked precursor oligomers bearing long alkyl chains and/or bulky substituents¹⁴ at some Por *meso*-positions. Using this strategy, Osuka *et al.* reported triply-fused Por dimers and trimers, dodecamers (Fig. 1a)¹³, and longer oligomers containing up to 24 Por units¹⁴, all of them obtained after a long multi-step synthesis in extremely low overall yields. Moreover, the low HOMO-LUMO gap of the resulting Por tapes led to severe stability issues, especially for the longest

oligomers. Additionally, the π -stacking tendency of these conjugates dramatically increases upon increasing the number of Por units, leading to solubility problems.

In the last decade, on-surface synthesis on atomically clean surfaces under ultra-high vacuum (UHV) conditions has emerged as an appealing alternative for the fabrication of planar, poorly soluble and inherently unstable π -conjugated systems^{19,20}. Moreover, the resulting on-surface synthesized nanostructures can be directly accessed by local-probe techniques such as scanning probe microscopy allowing for a detailed “*in situ*” structural and electronic characterization with molecular or even chemical bond resolution²¹. In the context of on-surface Por chemistry, many different systems have been prepared and studied, mainly involving one dimensional (1D) and two dimensional (2D) networks and their topological aspects^{22,23}. Regarding triply-fused Por systems, only porphine dimers²⁴ and Por dimers spaced by short graphene nanoribbon (GNR) segments^{25,26} have been reported. Meanwhile, the surface-assisted synthesis of triply-fused Por oligomers remains challenging and has not been achieved to date.

Herein, a simple, two-step strategy for the on-surface synthesis of laterally- π -extended Por nanotapes (NTs) is presented (Fig. 1b). The structural and electronic properties of individual Por NTs, both on Au(111) and NaCl/Au(111), have been scrutinized by high-resolution scanning probe microscopy/spectroscopy complemented with density functional theory calculations. Remarkably, the fabricated Por NTs feature magnetic end states resulting from the presence of an unpaired electron at each end of the Au(111)-supported NTs.

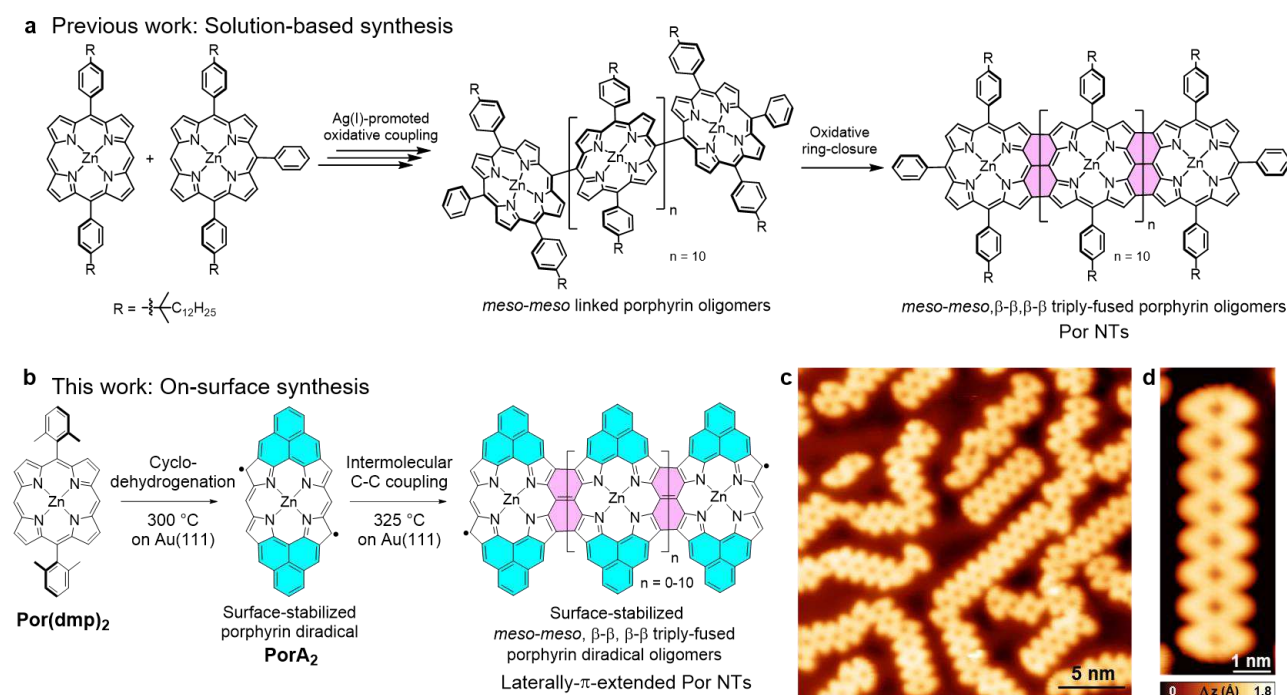


Fig. 1 | Synthesis of Por NTs. **a** Solution-based multi-step synthesis of Por NTs as reported by Osuka and co-workers¹³. **b** Two-step, on-surface synthesis of laterally- π -extended Por NTs on Au(111). **c** Overview STM image of the on-surface synthesis of Por NTs ($V_s = -0.5$ V, $I_t = 40$ pA). **d** Zoom-in STM image of **Por₈ NT** ($V_s = -0.06$ V, $I_t = 160$ pA).

On-surface synthesis of Por NTs

The synthetic route employed for the fabrication of surface-supported laterally π -extended Por NTs starts with **Por(dmp)₂** which was synthesized in few steps by solution chemistry²⁷. Sublimation of the latter Por on clean Au(111) under UHV conditions followed by thermal activation at 300 °C afforded two-fold phenalenyl-fused Por derivative **PorA₂** *via* surface-assisted cyclodehydrogenation²⁷. **PorA₂** exhibits a diradical open-shell character with two unpaired electrons delocalized over the Por longer “edges”. Despite their delocalization, the reactivity of these radicals is particularly high at the Por β -pyrrolic positions, as demonstrated by the formation of β -hydrogenated Por species²⁷. Taking into account that surface-stabilized radicals are key intermediates for the on-surface Ullmann-type coupling reaction, we decided to explore the possible thermally-activated polymerization of **PorA₂**. Indeed, further annealing of **PorA₂** at 325 °C triggered the formation of oligomeric Por species, namely Por NTs, in which **PorA₂** units are *meso-meso*, β - β , β - β triply-fused (Fig. 1c).

A typical STM image of a sample prepared through this two-step annealing is shown in Fig. 1c, and reveals several linear, *meso-meso*, β - β , β - β triply-fused Por NTs such as a **Por₈ NT** (Fig. 1d). Longer tapes containing up to 12 triply-fused Pors (**Por₁₂ NT**) could also be obtained (Supplementary Fig. S1.0). Moreover, the presence of some “ill-formed” Por NTs is observed, resulting from the fusion between the phenalenyl edge and the Por edge and/or the β -*meso* Por linkage, both of which arise from the delocalized nature of the radical. In the following, we focus exclusively on the main products, the linearly fused, regular Por NTs.

High-resolution STM and bond-resolved nc-AFM imaging²¹ have been carried out for a series of Por NTs with different numbers of constituting Por units (Figs. 2a and 2b). The corresponding nc-AFM images unequivocally prove the triple fusion between adjacent Pors in the NTs by evidencing the formation of three new C–C bonds between neighboring Por units. As demonstrated in our earlier work, the phenalenyl moieties confer an open-shell character to **PorA₂**, which gives rise to low-bias spectroscopy features²⁷. Therefore, the question arises whether the open-shell character is preserved for oligomeric Por NTs. To address this question, chemical structure analysis was initially performed, which suggests that, as in the case of **PorA₂**, no Kekulé resonance structures can be drawn for Por NTs (Supplementary Fig. S1.4). Among the possible resonance structures, the one which shows the

maximum number of Clar sextets and minimum number of unpaired electrons (*i.e.*, 2) – as the one drawn in Fig. 1b – can be expected to contribute most to the electronic structure.

In analogy to **PorA₂**, the unpaired electrons in Por NTs give rise to a higher reactivity, making the termini susceptible to hydrogenation²⁷, which can be demonstrated by nc-AFM imaging thanks to the extreme sensitivity of this technique to the apparent height of the adsorbates²⁸. Indeed, a close inspection of the Por tapes by constant-height nc-AFM imaging reveals doubly hydrogenated carbon atoms (CH₂) at the terminal β positions of some of the tapes (Supplementary Fig. S1.1). Using the same STM tip induced atomic manipulation protocol as for the hydrogenated **PorA₂** monomer²⁷, we could selectively transform the terminal C(sp₃)H₂ into C(sp₂)H, thereby removing the “extra” hydrogen atom (Fig. S1.1).

The unpaired electron at each end of the finite Por NTs indicates a localized spin $S = 1/2$, which may give rise to a many-body Kondo resonance originating from the screening of the localized spin by itinerant electrons from the underlying metal surface²⁹. To explore this scenario, we have performed differential conductance (dI/dV) spectroscopy over Por NTs of different lengths (Figs. 2e and 3). Sharp resonances around zero bias are indeed observed for all the tapes investigated pointing at the presence of the Kondo effect. We find that this zero-bias resonance is suppressed upon hydrogenation of the corresponding terminal β position, further confirming the $S = 1/2$ nature of the spin at the edge (Supplementary Fig. S1.1c). Constant-height STM imaging at -5 mV reveals the spatial distribution of the Kondo resonance which is localized over both ends of the Por tapes (Fig. 2c).

To gain further insight into the magnetic properties of the Por NTs, we have performed spin-polarized DFT calculations of free-standing Por NTs, which also demonstrate a spin-polarized ground state of the tapes with a net magnetic moment of $1 \mu_B$ ($S = 1/2$) at each end. The DFT-computed spin density maps of the corresponding tapes are displayed in Fig. 2d, and show excellent agreement with the experimental Kondo maps in Fig. 2c. The computed exchange coupling strength decreases with increasing length of the tapes, from 1.3 meV for **Por₂** NT, 0.2 meV for **Por₃** NT, to below the computational precision for longer Por NTs. We do not observe any inelastic spin excitation next to the Kondo resonance as previously reported in similar systems with exchange-coupled spins²⁷, which we attribute to the relatively broad Kondo peak and the low exchange coupling strength of 1.3 meV or less as evaluated from broken-symmetry solutions of the DFT calculations.

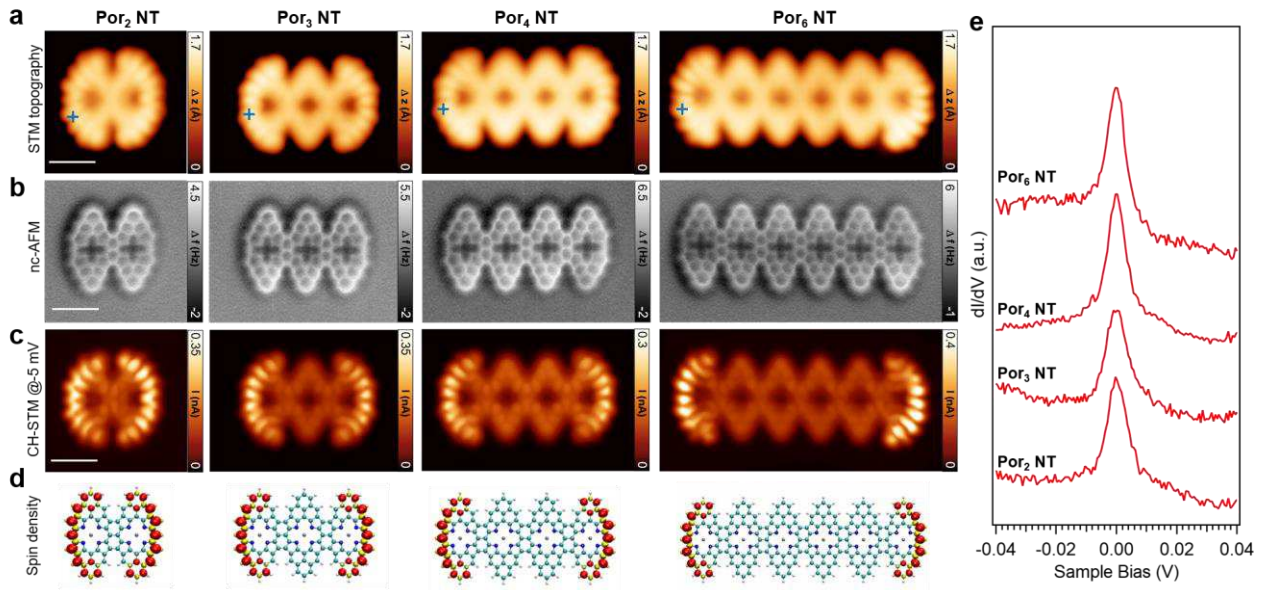


Fig. 2 | On-surface characterization of Por NTs. **a** Topographic STM images, **b** constant-height nc-AFM, and **c** simultaneously acquired constant-height STM image ($V_s = -0.005$ V) showing the spatial distribution of the Kondo resonance for **Por₂ NT**, **Por₃ NT**, **Por₄ NT**, and **Por₆ NT**, respectively. A CO-functionalized tip was used. Set points: **a** from left to right: $V_s = -0.06$ V, $I_t = 100$ pA; $V_s = -0.06$ V, $I_t = 220$ pA; $V_s = -0.06$ V, $I_t = 220$ pA; $V_s = -0.1$ V, $I_t = 120$ pA. Scale bars: 1 nm. **d** DFT computed spin densities of Por NTs imaged in **a**. **e**, dI/dV spectra acquired at the end of the Por NTs imaged in **a** (blue crosses), revealing Kondo resonances for all the tapes (Set points: $V_s = -0.06$ V, $I_t = 300$ pA, $V_{\text{mod}} = 1$ mV).

The observed Kondo resonances can be nicely fit with a Frota function^{30,31}, from which the resonance width (half width at half maximum, HWHM) can be determined (Fig. 3b). The energy scale of the Kondo effect is typically expressed by the Kondo temperature T_K , which is directly related to the width of the Kondo resonance. At lower temperatures ($T < T_K$), the Kondo resonance lies in the strong coupling regime and exhibits characteristic temperature-dependent broadening following the Fermi-liquid model³². In Fig. 3b,c, we report the temperature evolution of the Kondo resonance at the end of **Por₇ NT**. By fitting the HWHM Γ of the resonances with the Fermi-liquid model $\Gamma = \frac{1}{2} \sqrt{(\alpha k_B T)^2 + (2k_B T_K)^2}$, we obtained a Kondo temperature $T_K = 49.9 \pm 3.3$ K, and a multiplicative factor $\alpha = 10.8 \pm 0.4$.

1D organic structures with unpaired electrons and thus localized spins at their termini have also been observed in armchair graphene nanoribbons (AGNRs) with zigzag type ends³³. When these AGNRs

are directly adsorbed on the metal surface, charge transfer to the metal empties the singly-occupied end states. However, the termini of AGNRs with a transverse width of 7 carbon atoms (7AGNR) clearly display spin-split end states after being transferred onto a thin insulating film ("decoupling layer")³³. 5AGNRs are also predicted to host localized magnetic moments at their termini, and a zero-bias resonance in STM-based transport spectra has indeed been detected for 5AGNRs with one of their termini located on a decoupling layer³⁴. Furthermore, localized end states featuring zero-bias resonances have been observed for an ethynylene-bridged anthracene polymer³⁵. Such localized end states are gaining increasing interest due to their origin in topologically non-trivial electronic quantum phases, and because they may find applications in future quantum devices³⁶.

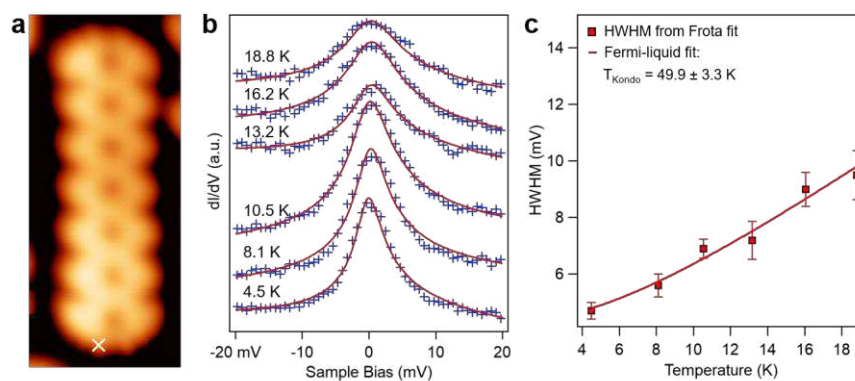


Fig. 3 | Kondo temperature of the end-localized spins. **a** STM image of Por₇ NT ($V_s = -0.05$ V, $I_t = 320$ pA). **b** Temperature evolution of the Kondo spectra, with the experimental data (blue crosses) fit by the Frota function (red curves). Data have been acquired at the position marked by a cross in **a** ($V_{\text{mod}} = 0.8$ mV). **c** Extracted half width at half maximum (HWHM) of the Kondo resonance as a function of temperature. The data are fit by the Fermi-liquid model to determine the Kondo temperature.

Due to electron correlations, the unpaired electrons at the two ends of the Por NTs are expected to result in spin-polarized singly occupied and unoccupied molecular orbitals (SOMO and SUMO, respectively)³⁷. To prevent orbital hybridization with the underlying metal surface (and thus to enable probing of intrinsic electronic properties), a common strategy is to intercalate a thin insulating film between the molecules and the metal surface^{33,34,37}. Following the formation of the Por NTs, we therefore deposited a submonolayer of NaCl onto the samples, which led to bilayer islands of (001)-terminated NaCl on parts of the Au(111) surface. STM manipulation was thereafter applied to transfer Por NTs onto such a NaCl island (Figs. 4a and 4b). An enhanced contribution of electronic frontier states to STM images immediately indicates an efficient electronic decoupling of the Por NT from the metal substrate (Fig. 4d). Meanwhile, at lower bias voltages where there are no molecular states

accessible, only the molecular skeletons are visible from the STM images (Fig. 4c). We have first examined the low-bias dI/dV spectra at the ends of Por NTs of different lengths (Fig. 4c), where no Kondo-like features are observed as expected due to the absence of conduction electrons in the underlying NaCl island. Wide-range dI/dV and the concomitant current spectra have been acquired on the Por NTs to access their molecular orbitals (**Por₅ NT** in Fig. 4e, and **Por₄ NT** in Supplementary Fig. S1.2). The spectra acquired at the end of the Por NTs display a broad gap region of low conductance (red line in I/V spectrum, Fig. 4e) and broad peaks at around -0.4 V and 1.0 V (red line in dI/dV spectrum, Fig. 4e), respectively. Meanwhile, the spectra taken at the central part of the Por NT exhibit three characteristic broad peaks, the first one at negative bias in proximity to that of the end, the second one at a small positive bias centered around 0.2 V, and the third one pronounced at 1.1 V.

Spin-polarized DFT calculations of molecular orbitals and energy levels of **Por₅ NT** in gas phase were performed to make a direct comparison to the experimental results (the frontier orbitals and their notations are indicated in Fig. 4g). From theory, two spin-split singly occupied and unoccupied molecular orbitals ($SOMO^\uparrow/SOMO^\downarrow$ and $SUMO^\uparrow/SUMO^\downarrow$, respectively) localized at both termini of the tape are discerned. The energy difference between SOMO and SUMO states is 0.46 eV and independent of the length of the tape (Supplementary Fig. S1.6), as is expected for a Coulomb gap (originating from electron correlation) and in contrast to what would be expected for a hybridization gap. The SUMO is in excellent agreement with the STS map of the tape at 1 V, while due to the close energetic proximity of SOMO and HOMO-1 the STS map at -0.4 V comprises contributions from both (Fig. 4f). Therefore, based on the dI/dV spectra acquired at the end of the tape and the STS maps at characteristic energies, we assign the states at -0.4 V and 1.0 V to the SOMO and SUMO, respectively. Moreover, the state at 1.1 V clearly derives from the LUMO (Figs. 4e-g). Finally, the state at 0.3 V can be assigned to the HOMO which is delocalized over the central part of the tape (Figs. 4f and 4g), suggesting that the **Por₅ NT** is (positively) charged on NaCl/Au(111), as has also been observed for short 5AGNRs on NaCl/Au(111)³⁴. However, because the SOMO lies lower in energy than the HOMO (Fig. 4g), the spin-split end states $SOMO^\uparrow/SOMO^\downarrow$ and $SUMO^\uparrow/SUMO^\downarrow$ are preserved despite the depopulation of the HOMO due to charge transfer. We note a somewhat asymmetric shape of the left and right parts of the tape ends in STM images, which are also present in all the STS maps, which we attribute to some degree of hybridization and the registry of the Por NT to the underlying NaCl.

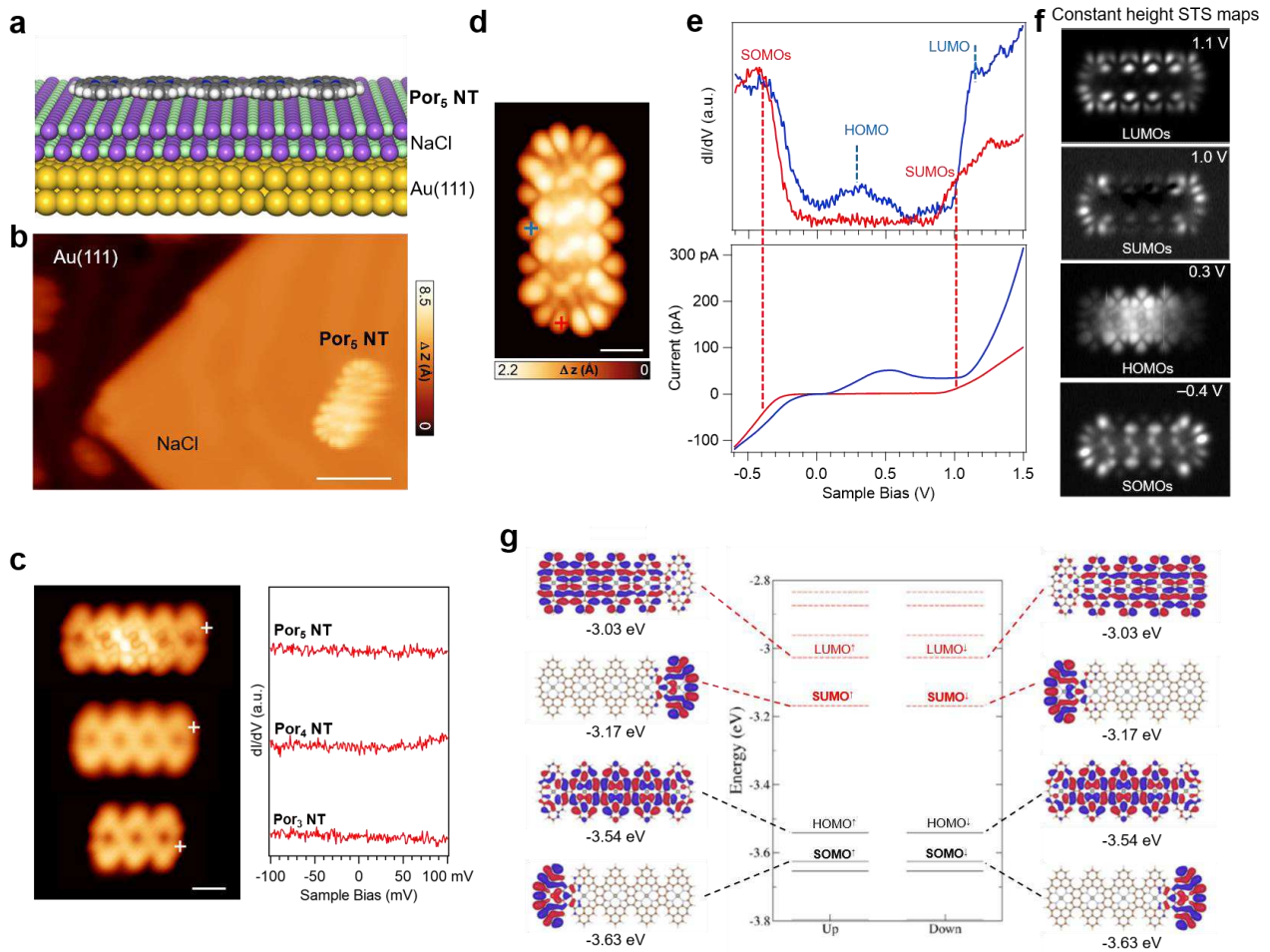


Fig. 4 | Electronic decoupling of Por NTs from Au(111). **a** Schematic model illustrating **Por₅ NT** on a thin insulating NaCl bilayer supported by Au(111). **b** STM image of **Por₅ NT** transferred onto NaCl/Au(111) ($V_s = -0.2$ V, $I_t = 12$ pA). Scale bar: 4 nm. **c**, (Left) STM images of **Por₅ NT** pentamer, **Por₄ NT** tetramer, and **Por₃ NT** trimer (from top to bottom) on NaCl/Au(111), and (right) the corresponding low-energy dI/dV spectra acquired at their termini (positions indicated by white crosses in **c**). Set points: for **Por₅ NT**: $V_s = -0.1$ V, $I_t = 20$ pA; for **Por₄ NT**: $V_s = -0.1$ V, $I_t = 8$ pA; for **Por₃ NT**: $V_s = 0.1$ V, $I_t = 6$ pA. Scale bar: 1 nm. **d**, STM image of **Por₅ NT** on NaCl/Au(111) ($V_s = -0.6$ V, $I_t = 120$ pA). Scale bar: 1 nm. **e**, Differential conductance dI/dV and simultaneously acquired current (I/V) spectra recorded over the **Por₅ NT** (acquisition positions indicated by crosses in **c**). **f**, Constant-height STS maps at different bias voltages, as indicated. Set points from top to bottom: $V_s = 0.1$ V, $I_t = 6$ pA; $V_s = 0.1$ V, $I_t = 6$ pA; $V_s = 0.1$ V, $I_t = 6$ pA; $V_s = -0.1$ V, $I_t = 6$ pA. **g**, Spin-polarized DFT calculated molecular orbitals and energy levels of **Por₅ NT** in gas phase (the antiferromagnetic case is shown). There are two degenerate SOMO and SUMO states, which are spatially located at the ends of the tape. SOMO is found to be shifted below the HOMO of the **Por₅ NT**.

Hitherto reported triply-linked Por NTs have shown remarkable electronic properties and low frontier orbital gaps which makes them promising candidates for molecular electronics applications^{13,38}. To characterize the frontier orbital gaps of our Por NTs in contact with a metal electrode, we have carried out STS experiments on Por NTs adsorbed on Au(111) complemented by DFT calculations. Interestingly, our DFT calculations for a free-standing infinite Por NT yield a gap of 0.46 eV (Supplementary Fig. S1.3), which is higher than the one of 0.08 eV reported for a Por tape without phenalenyl π -extension at a similar level of theory³⁸. Nevertheless the electronic band gap of our Por tapes is still comparably small for a 1D organic system (for comparison, the band gap of the "quasi"-metallic 5AGNR is about 0.42 eV by DFT)³⁹. Experimentally, the gap of **Por₆ NT** and longer Por NTs on Au(111) is determined to be 0.9 eV (see discussion in Supplementary Fig. S1.5).

Conclusions

We have reported a facile on-surface route towards the preparation of *meso-meso*, β - β , β - β triply-linked Por NTs, which uses a surface-stabilized π -extended diradical **PorA₂** as molecular building block. The atomic structure and electronic features of such surface-supported architectures, both on Au(111) and on a thin insulating NaCl layer, were studied by means of high-resolution scanning probe microscopy and DFT calculations. Notably, the open-shell character of **PorA₂** is retained in the Por NTs, which host one unpaired electron at each end.

The presented straightforward fabrication of Por NTs paves the way towards the realization of appealing surface-supported architectures by the complexation of magnetically active metal ions within the inner Por cavity. In this context, applications such as 1D spin filters, sensors, or catalysis can be envisioned. Moreover, the Por NTs provide a scaffold that allows the arrangement of several magnetic ions at a close distance, thereby allowing their interactions. This, together with the inherent open-shell character of the tapes, may lead to exotic physical phenomena and quantum applications, which go beyond the actively explored pure carbon-based 1D magnetic systems³⁴⁻³⁶.

Methods

STM/STS and nc-AFM characterization. A commercial low-temperature STM/AFM (Scienta Omicron) system was used for sample preparation and *in situ* characterization under ultra-high vacuum conditions (base pressure below 1×10^{-10} mbar). Au(111) single crystal substrates were cleaned by standard argon sputtering and annealing cycles. Deposition of the molecular precursors was carried out by thermal evaporation from a 6-fold organic evaporator (Mantis GmbH). STM images were recorded in constant-current mode unless otherwise stated, and the dI/dV spectra and

maps were recorded using the lock-in technique ($U_{\text{rms}} = 20$ mV if not otherwise specified). All the measurements were carried out at 4.8 K.

Theoretical method. Density functional theory calculations were performed with the VASP code⁴⁰ using the PBE exchange and correlation functional⁴¹. Core electrons were treated within the projector augmented method^{42,43} and wavefunctions were expanded using a planewave basis set with an energy cutoff of 400 eV. The (111) surface of Au was simulated using a 4 layer slab and a *vacuum* gap of 18 Å. The two bottom layers of Au were kept fixed and all the other atoms were relaxed until forces were smaller than 0.02 eV/Å (0.001 eV/Å for the gas-phase calculations). A (03 × 01 × 01) k-grid mesh was used in the relaxations, which was increased to (07 × 02 × 01) for the simulations of STM images and dI/dV maps. Van der Waals interactions have been included using the Tkatchenko-Scheffler scheme⁴⁴. STM simulated images have been simulated within the Tersoff-Hamann method⁴⁵ as described by Bocquet *et al.*⁴⁶ and implemented in the STMpw program⁴⁷. Images of the structures and isosurfaces were plotted using VESTA⁴⁸.

Acknowledgements

This work was supported by the Swiss National Science Foundation under Grant No. 200020_182015, the European Union's Horizon 2020 research and innovation programme under grant agreement number 785219 (Graphene Flagship Core 2), the Office of Naval Research (N00014-18-1-2708), MINECO, CTQ2017-85393-P (Phthalophoto, TT), and CTQ-2020 (Porphyrinoids, TT, GB). IMDEA Nanociencia also acknowledges support from the 'Severo Ochoa' Programme for Centres of Excellence in R&D (MINECO, Grant SEV-2016-0686). R.R. and N.L. are grateful for funding from the EU-FET Open H2020 Mechanics with Molecules project (grant 766864).

Author Contributions

Q.S. performed the on-surface synthesis and spectroscopy measurements under the supervision of P.R. and R.F.. L.M.M. synthesized the molecular precursors, under the supervision of T.T. and G.B.. R.R. and N.L. carried out the DFT calculations. Q.S., L.M.M., G.B., and R.R. wrote the paper with contributions from all coauthors. All authors discussed the results and commented on the manuscript at all stages.

Competing financial interests

The authors declare no competing financial interests.

References

1. Kadish KM, Smith KM, Guillard R (eds). *The porphyrin handbook*. Academic Press: Burlington, MA, 2000.
2. Urbani M, Grätzel M, Nazeeruddin MK, Torres T. *Meso*-substituted porphyrins for dye-sensitized solar cells. *Chem. Rev.* **114**, 12330-12396 (2014).
3. Beyene BB, Hung C-H. Recent progress on metalloporphyrin-based hydrogen evolution catalysis. *Coord. Chem. Rev.* **410**, 213234 (2020).
4. Jurow M, Schuckman AE, Batteas JD, Drain CM. Porphyrins as molecular electronic components of functional devices. *Coord. Chem. Rev.* **254**, 2297-2310 (2010).
5. Winters MU, Dahlstedt E, Blades HE, Wilson CJ, Frampton MJ, *et al.* Probing the efficiency of electron transfer through porphyrin-based molecular wires. *J. Am. Chem. Soc.* **129**, 4291-4297 (2007).
6. Sedghi G, García-Suárez VM, Esdaile LJ, Anderson HL, Lambert CJ, *et al.* Long-range electron tunnelling in oligo-porphyrin molecular wires. *Nat. Nanotechnol.* **6**, 517 (2011).
7. Lewtak JP, Gryko DT. Synthesis of π -extended porphyrins *via* intramolecular oxidative coupling. *Chem. Commun.* **48**, 10069-10086 (2012).
8. Cho WJ, Cho Y, Min SK, Kim WY, Kim KS. Chromium porphyrin arrays as spintronic devices. *J. Am. Chem. Soc.* **133**, 9364-9369 (2011).
9. Tanaka T, Osuka A. Conjugated porphyrin arrays: Synthesis, properties and applications for functional materials. *Chem. Soc. Rev.* **44**, 943-969 (2015).
10. Sedghi G, Esdaile LJ, Anderson HL, Martin S, Bethell D, *et al.* Comparison of the conductance of three types of porphyrin-based molecular wires: β ,*meso*, β -Fused tapes, *meso*-butadiyne-linked and twisted *meso-meso* linked oligomers. *Adv. Mater.* **24**, 653-657 (2012).
11. Anderson HL. Building molecular wires from the colours of life: Conjugated porphyrin oligomers. *Chem. Commun.* 2323-2330 (1999).
12. Arnold DP. Two rings are better than one: Adventures in porphyrin chemistry. *Synlett* **2000**, 296-305 (2000).
13. Tsuda A, Osuka A. Fully conjugated porphyrin tapes with electronic absorption bands that reach into infrared. *Science* **293**, 79-82 (2001).
14. Ikeda T, Aratani N, Osuka A. Synthesis of extremely π -extended porphyrin tapes from hybrid *meso-meso* linked porphyrin arrays: An approach towards the conjugation length. *Chem. Asian J.* **4**, 1248-1256 (2009).
15. Leary E, Limburg B, Alanazy A, Sangtarash S, Grace I, *et al.* Bias-driven conductance increase with length in porphyrin tapes. *J. Am. Chem. Soc.* **140**, 12877-12883 (2018).
16. Sikes HD, Smalley JF, Dudek SP, Cook AR, Newton MD, *et al.* Rapid electron tunneling through oligophenylenevinylene bridges. *Science* **291**, 1519-1523 (2001).
17. Yamada R, Kumazawa H, Noutoshi T, Tanaka S, Tada H. Electrical conductance of oligothiophene molecular wires. *Nano Lett.* **8**, 1237-1240 (2008).

18. Wang C, Batsanov AS, Bryce MR, Martín S, Nichols RJ, *et al.* Oligoynne single molecule wires. *J. Am. Chem. Soc.* **131**, 15647-15654 (2009).
19. Sun Q, Zhang R, Qiu J, Liu R, Xu W. On-surface synthesis of carbon nanostructures. *Adv. Mater.* **30**, 1705630 (2018).
20. Clair S, de Oteyza DG. Controlling a chemical coupling reaction on a surface: Tools and strategies for on-surface synthesis. *Chem. Rev.* **119**, 4717-4776 (2019).
21. Gross L, Mohn F, Moll N, Liljeroth P, Meyer G. The chemical structure of a molecule resolved by atomic force microscopy. *Science* **325**, 1110-1114 (2009).
22. Auwärter W, Écija D, Klappenberger F, Barth JV. Porphyrins at interfaces. *Nat. Chem.* **7**, 105-120 (2015).
23. Gottfried JM. Surface chemistry of porphyrins and phthalocyanines. *Surf. Sci. Rep.* **70**, 259-379 (2015).
24. Wiengarten A, Seufert K, Auwärter W, Ecija D, Diller K, *et al.* Surface-assisted dehydrogenative homocoupling of porphine molecules. *J. Am. Chem. Soc.* **136**, 9346-9354 (2014).
25. Mateo LM, Sun Q, Liu S-X, Bergkamp JJ, Eimre K, *et al.* On-surface synthesis and characterization of triply fused porphyrin–graphene nanoribbon hybrids. *Angew. Chem. Int. Ed.* **59**, 1334-1339 (2020).
26. Mateo LM, Sun Q, Eimre K, Pignedoli CA, Torres T, *et al.* On-surface synthesis of singly and doubly porphyrin-capped graphene nanoribbon segments. *Chem. Sci.* **12**, 247-252 (2021).
27. Sun Q, Mateo LM, Robles R, Ruffieux P, Lorente N, *et al.* Inducing open-shell character in porphyrins through surface-assisted phenalenyl π -extension. *J. Am. Chem. Soc.* **142**, 18109-18117 (2020).
28. Majzik Z, Pavliček N, Vilas-Varela M, Pérez D, Moll N, *et al.* Studying an antiaromatic polycyclic hydrocarbon adsorbed on different surfaces. *Nat. Commun.* **9**, 1198 (2018).
29. Ternes M, Heinrich AJ, Schneider W-D. Spectroscopic manifestations of the Kondo effect on single adatoms. *J. Phys.: Condens. Matter* **21**, 053001 (2008).
30. Frota HO. Shape of the Kondo resonance. *Phys. Rev. B* **45**, 1096-1099 (1992).
31. Prüser H, Dargel PE, Bouhassoune M, Ulbrich RG, Pruschke T, *et al.* Interplay between the Kondo effect and the Ruderman–Kittel–Kasuya–Yosida interaction. *Nat. Commun.* **5**, 5417 (2014).
32. Nagaoka K, Jamneala T, Grobis M, Crommie MF. Temperature dependence of a single Kondo impurity. *Phys. Rev. Lett.* **88**, 077205 (2002).
33. Wang S, Talirz L, Pignedoli CA, Feng X, Müllen K, *et al.* Giant edge state splitting at atomically precise graphene zigzag edges. *Nat. Commun.* **7**, 11507 (2016).
34. Lawrence J, Brandimarte P, Berdonces-Layunta A, Mohammed MSG, Grewal A, *et al.* Probing the magnetism of topological end states in 5-armchair graphene nanoribbons. *ACS Nano* **14**, 4499-4508 (2020).
35. Cirera B, Sánchez-Grande A, de la Torre B, Santos J, Edalatmanesh S, *et al.* Tailoring topological order and π -conjugation to engineer quasi-metallic polymers. *Nat. Nanotechnol.* **15**, 437-443 (2020).

36. Cao T, Zhao F, Louie SG. Topological phases in graphene nanoribbons: Junction states, spin centers, and quantum spin chains. *Phys. Rev. Lett.* **119**, 076401 (2017).
37. Sun Q, Yao X, Gröning O, Eimre K, Pignedoli CA, *et al.* Coupled spin states in armchair graphene nanoribbons with asymmetric zigzag edge extensions. *Nano Lett.* **20**, 6429-6436 (2020).
38. Kang H, Kim Y-S. Electronic and quantum transport properties of heterobilayers of graphene nanoribbons and zinc-porphyrin tapes. *J. Phys. Chem. C* **116**, 8167-8173 (2012).
39. Yang L, Park C-H, Son Y-W, Cohen ML, Louie SG. Quasiparticle energies and band gaps in graphene nanoribbons. *Phys. Rev. Lett.* **99**, 186801 (2007).
40. Kresse G, Furthmüller J. Efficiency of *ab-initio* total energy calculations for metals and semiconductors using a plane-wave basis set. *Comput. Mater. Sci.* **6**, 15-50 (1996).
41. Perdew JP, Burke K, Ernzerhof M. Generalized gradient approximation made simple. *Phys. Rev. Lett.* **77**, 3865-3868 (1996).
42. Kresse G, Joubert D. From ultrasoft pseudopotentials to the projector augmented-wave method. *Phys. Rev. B* **59**, 1758-1775 (1999).
43. Blöchl PE. Projector augmented-wave method. *Phys. Rev. B* **50**, 17953-17979 (1994).
44. Tkatchenko A, Scheffler M. Accurate molecular van der waals interactions from ground-state electron density and free-atom reference data. *Phys. Rev. Lett.* **102**, 073005 (2009).
45. Tersoff J, Hamann DR. Theory of the scanning tunneling microscope. *Phys. Rev. B* **31**, 805-813 (1985).
46. Bocquet M-L, Lesnard H, Monturet S, Lorente N. Theory of elastic and inelastic electron tunneling. In: van Santen RA, Sautet P (eds). *Computational methods in catalysis and materials science*. Wiley-VCH Verlag GmbH & Co. KGaA, 2009, pp 199-219.
47. Lorente N, Robles R. (2019, December 17). Stmpw (v1.0b2). Zenodo. 10.5281/zenodo.3581159
48. Momma K, Izumi F. *VESTA* 3 for three-dimensional visualization of crystal, volumetric and morphology data. *J. Appl. Crystallogr.* **44**, 1272-1276 (2011).

Figures

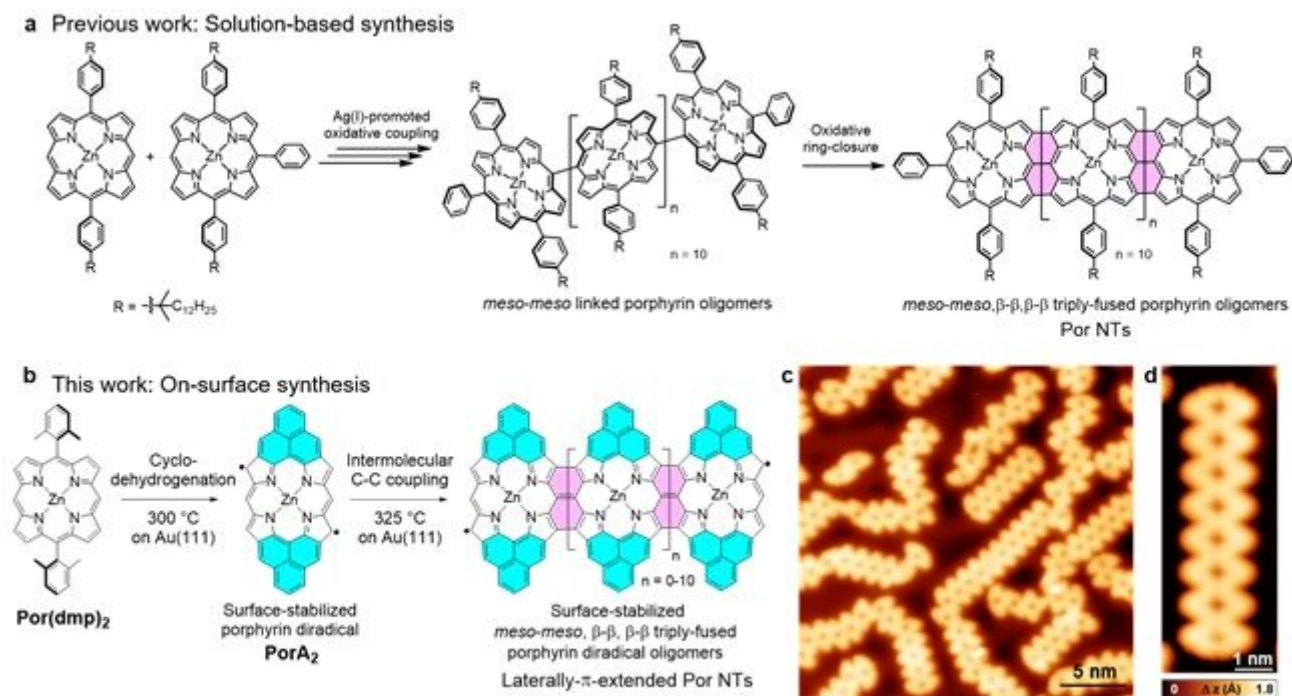


Figure 1

Synthesis of Por NTs. a Solution-based multi-step synthesis of Por NTs as reported by Osuka and co-workers¹³. b Two-step, on-surface synthesis of laterally- π -extended Por NTs on Au(111). c Overview STM image of the on-surface synthesis of Por NTs ($V_s = \pm 0.5$ V, $I_t = 40$ pA). d Zoom-in STM image of Por₈ NT ($V_s = \pm 0.06$ V, $I_t = 160$ pA).

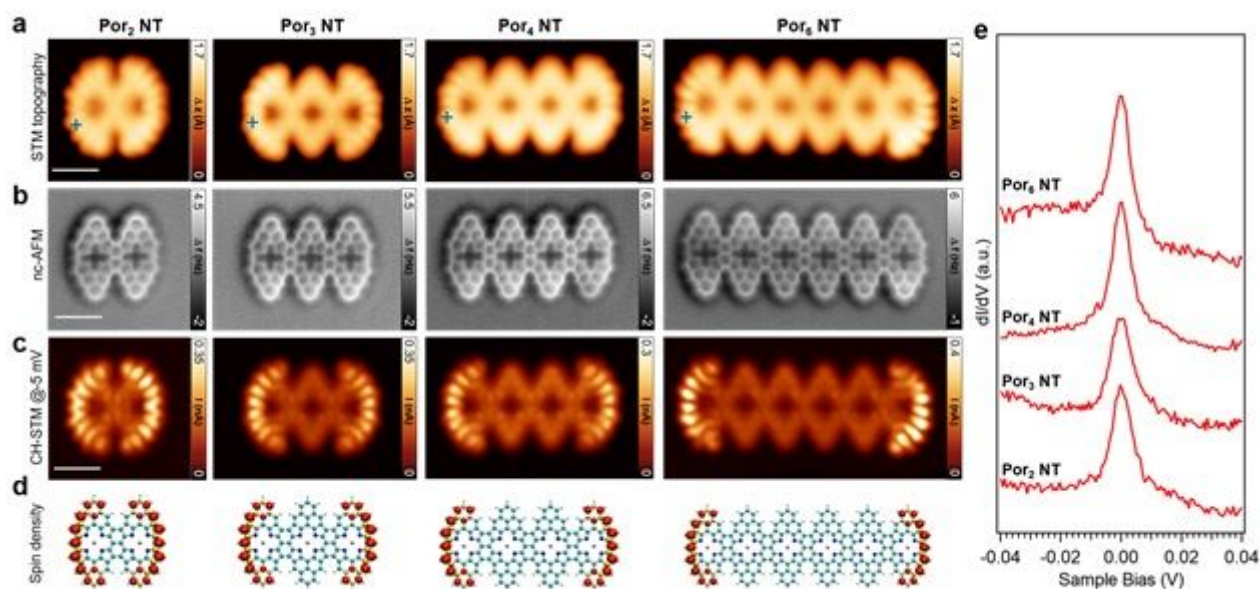


Figure 2

On-surface characterization of Por NTs. a Topographic STM images, b constant-height nc-AFM, and c simultaneously acquired constant-height STM image ($V_s = \pm 0.005$ V) showing the spatial distribution of the Kondo resonance for Por₂ NT, Por₃ NT, Por₄ NT, and Por₆ NT, respectively. A CO-functionalized tip was used. Set points: a from left to right: $V_s = \pm 0.06$ V, $I_t = 100$ pA; $V_s = \pm 0.06$ V, $I_t = 220$ pA; $V_s = \pm 0.06$ V, $I_t = 220$ pA; $V_s = \pm 0.1$ V, $I_t = 120$ pA. Scale bars: 1 nm. d DFT computed spin densities of Por NTs imaged in a. e, dI/dV spectra acquired at the end of the Por NTs imaged in a (blue crosses), revealing Kondo resonances for all the tapes (Set points: $V_s = \pm 0.06$ V, $I_t = 300$ pA, $V_{mod} = 1$ mV).

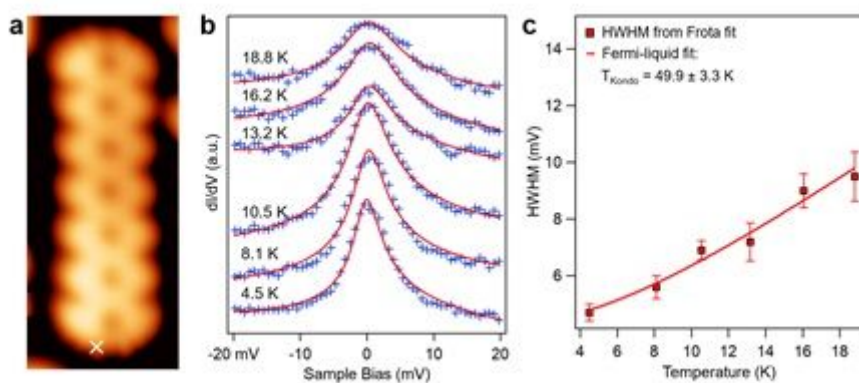


Figure 3

Kondo temperature of the end-localized spins. a STM image of Por₇ NT ($V_s = \pm 0.05$ V, $I_t = 320$ pA). b Temperature evolution of the Kondo spectra, with the experimental data (blue crosses) fit by the Frota function (red curves). Data have been acquired at the position marked by a cross in a ($V_{mod} = 0.8$ mV). c

Extracted half width at half maximum (HWHM) of the Kondo resonance as a function of temperature. The data are fit by the Fermi-liquid model to determine the Kondo temperature.

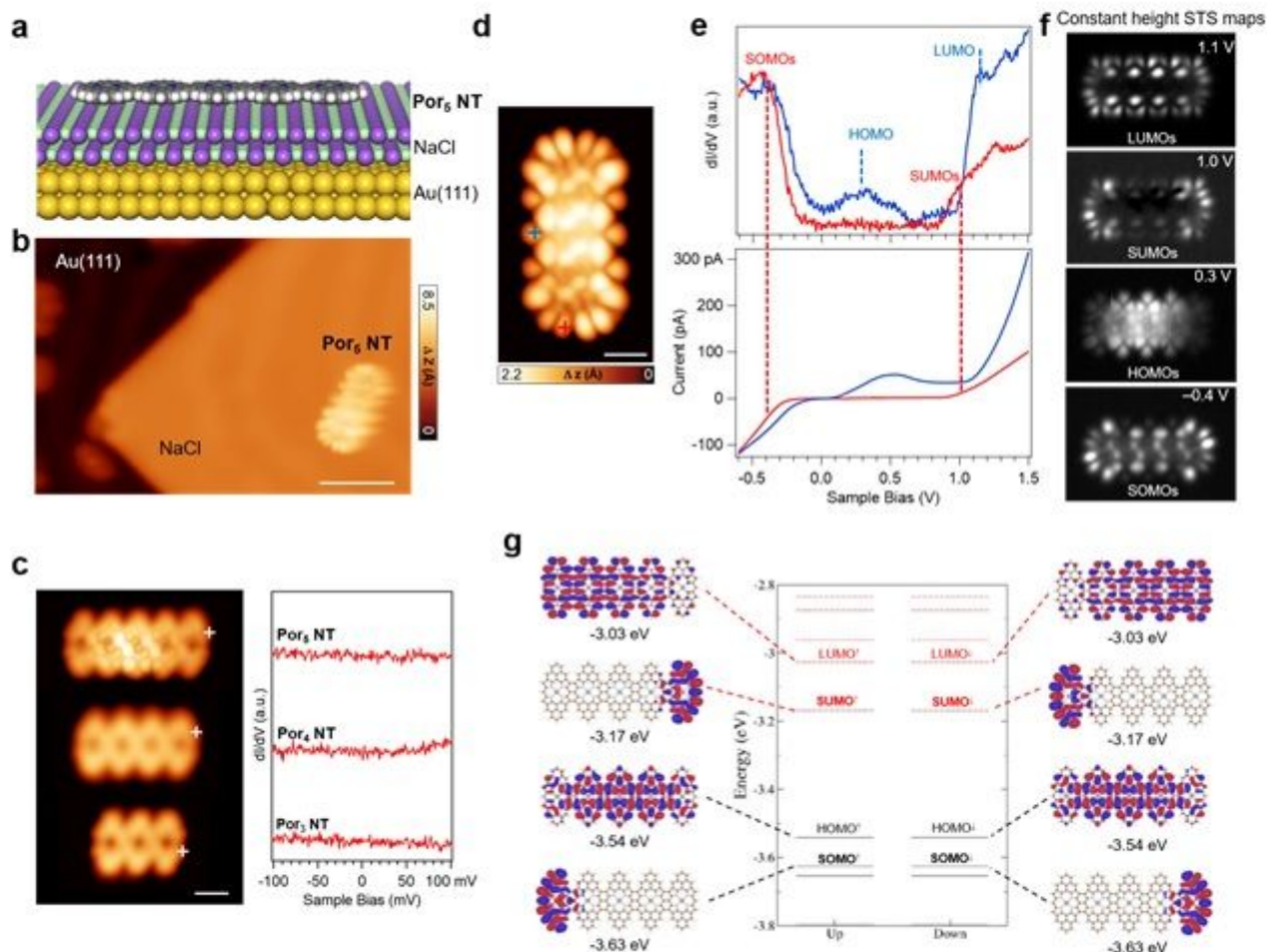


Figure 4

Electronic decoupling of Por NTs from Au(111). a Schematic model illustrating Por₅ NT on a thin insulating NaCl bilayer supported by Au(111). b STM image of Por₅ NT transferred onto NaCl/Au(111) ($V_s = \pm 0.2$ V, $I_t = 12$ pA). Scale bar: 4 nm. c, (Left) STM images of Por₅ NT pentamer, Por₄ NT tetramer, and Por₃ NT trimer (from top to bottom) on NaCl/Au(111), and (right) the corresponding low-energy dI/dV spectra acquired at their termini (positions indicated by white crosses in c). Set points: for Por₅ NT: $V_s = \pm 0.1$ V, $I_t = 20$ pA; for Por₄ NT: $V_s = \pm 0.1$ V, $I_t = 8$ pA; for Por₃ NT: $V_s = 0.1$ V, $I_t = 6$ pA. Scale bar: 1 nm. d, STM image of Por₅ NT on NaCl/Au(111) ($V_s = \pm 0.6$ V, $I_t = 120$ pA). Scale bar: 1 nm. e, Differential conductance dI/dV and simultaneously acquired current (I/V) spectra recorded over the Por₅ NT (acquisition positions indicated by crosses in c). f, Constant-height STS maps at different bias voltages, as indicated. Set points from top to bottom: $V_s = 0.1$ V, $I_t = 6$ pA; $V_s = 0.1$ V, $I_t = 6$ pA; $V_s = 0.1$ V, $I_t = 6$ pA; $V_s = -0.1$ V, $I_t = 6$ pA. g, Spin-polarized DFT calculated molecular orbitals and energy levels of Por₅ NT in gas phase (the antiferromagnetic case is shown). There are two degenerate SOMO and SUMO states,

which are spatially located at the ends of the tape. SOMO is found to be shifted below the HOMO of the Por5 NT.

Supplementary Files

This is a list of supplementary files associated with this preprint. Click to download.

- [ZnPorNanotapesSI.docx](#)